OPEN ACCESS
IOP Publishing
Nanotechnology

Nanotechnology **33** (2022) 415002 (7pp)
https://doi.org/10.1088/1361-6528/ac7c25

Evidence of decoupling of surface and bulk states in Dirac semimetal Cd_3As_2

W Yu[1], D X Rademacher[1], N R Valdez[1], M A Rodriguez[1], T M Nenoff[1] and W Pan[2]

[1] Sandia National Laboratories, Albuquerque, New Mexico NM-87185, United States of America
[2] Sandia National Laboratories, Livermore, California CA-94551, United States of America

E-mail: wpan@sandia.gov

Received 1 March 2022, revised 16 June 2022
Accepted for publication 27 June 2022
Published 25 July 2022

Abstract

Dirac semimetals have attracted a great deal of current interests due to their potential applications in topological quantum computing, low-energy electronic devices, and single photon detection in the microwave frequency range. Herein are results from analyzing the low magnetic (B) field weak-antilocalization behaviors in a Dirac semimetal Cd_3As_2 thin flake device. At high temperatures, the phase coherence length l_ϕ first increases with decreasing temperature (T) and follows a power law dependence of $l_\phi \propto T^{-0.4}$. Below ~3 K, l_ϕ tends to saturate to a value of ~180 nm. Another fitting parameter α, which is associated with independent transport channels, displays a logarithmic temperature dependence for $T > 3$ K, but also tends to saturate below ~3 K. The saturation value, ~1.45, is very close to 1.5, indicating three independent electron transport channels, which we interpret as due to decoupling of both the top and bottom surfaces as well as the bulk. This result, to our knowledge, provides first evidence that the surfaces and bulk states can become decoupled in electronic transport in Dirac semimetal Cd_3As_2.

Keywords: Dirac semimetal, surface and bulk states, weak anti-localization

(Some figures may appear in colour only in the online journal)

The discovery of topological materials [1–4] not only enriches our understanding of condensed matter physics, but also is promised to provide exciting new functionalities for future electronic applications. Many forms of topological materials have been predicted. Among them, Dirac semimetals [5, 6] have been prominent. In a Dirac semimetal, the conduction and valence bands meet at a single pair of three-dimensional (3D) degenerated Dirac points located at finite momentum points and display linear dispersion. The gapless crossing, even in the presence of strong spin–orbit interaction in Cd_3As_2, is protected by crystal symmetry. Shortly after the prediction of 3D topological Dirac semimetals, materials such as Cd_3As_2 were examined, for example, by angle-resolved photoemission spectroscopy [7–9] and scanning tunneling spectroscopy measurements [10] to reveal the Dirac points and linear energy dispersion.

One of the hallmarks of a Dirac semimetal is its unusual topological surface states, the Fermi arc states that connect the projections of the bulk Dirac points on the sample surfaces. Studies of these surface states have generated a great deal of interests in recent years [11–17]; they are a promising candidate for realizing Majorana quasiparticles [18, 19] for fault tolerant topological quantum computing [20] and for single photon detection in the microwave frequency range [21]. Recent experiments on dc (direct current) and ac (alternating current) Josephson effects in superconductor-Cd_3As_2-superconductor Josephson junctions have shown clear signatures of superconducting topological surface states [11–14]. Moreover, these Josephson effects strongly suggest that there exists a π phase difference between the superconducting surface and bulk states [11]. The exact origin of this π-phase difference is not known at present. As such, it is important to understand electronic transport properties of these surface and bulk states.

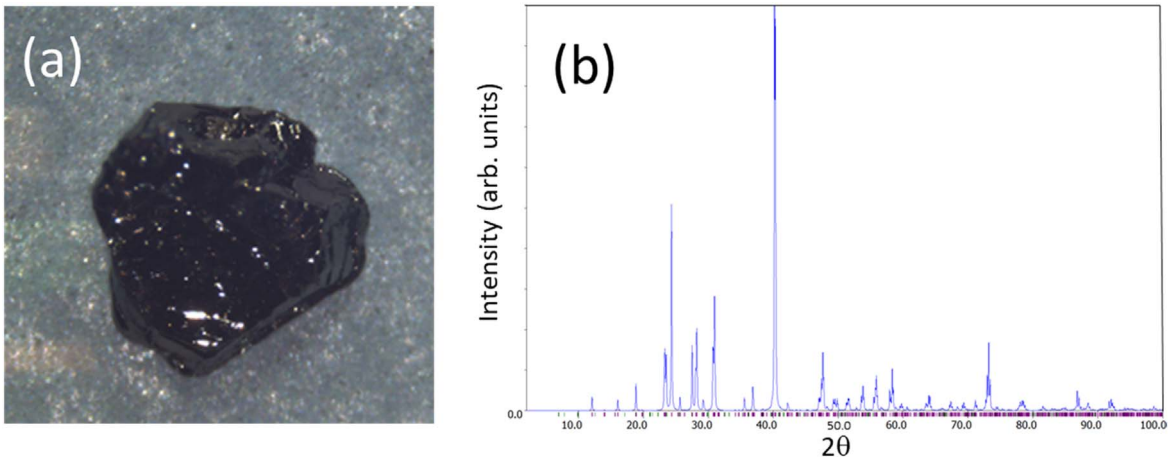

Figure 1. (a) Optical image of an as-grown Cd_3As_2 ingot. (b) Powder XRD plot simulated using single crystal data.

The weak antilocalization (WAL) effect has commonly been used to examine the coupling/decoupling of the surface and bulk states in topological quantum materials [22–42]. In a system with spin-momentum locking and the resulting π Berry phase, the constructive interference of two time-reversal paths gives rise to a magnetoconductivity correction (equation (1)) [26, 34, 43] as follows:

$$\Delta\sigma(B) = \sigma_{XX}(B) - \sigma_{XX}(0) = \alpha \times (e^2/\pi h) f(B_\phi/B), \quad (1)$$

where $\sigma_{xx}(B)$ is the conductivity at a magnetic field of B, $\sigma_{xx}(0)$ the conductivity at $B = 0$, e the electron charge, h the Planck constant, $f(x) \equiv \ln(x) - \Psi(1/2 + x)$ with Ψ being the digamma function. B_ϕ is the magnetic field associated with the phase coherence length $l_\phi = (\hbar/eB_\phi)^{1/2}$. α is related to the number of independent transport channels. In previous studies on WAL in topological insulators, such as Bi_2Se_3, α is determined by coupling/decoupling of the surfaces and bulk [26, 28–33, 38]. When the surfaces and bulk are strongly coupled, they are treated as one coherent channel and $\alpha = 0.5$. When the top and bottom surfaces are decoupled from the bulk, $\alpha = 1$ due to the existence of two independent channels.

The WAL effect in Dirac semimetal Cd_3As_2 has also been studied by a few groups. The results, particularly the value of α, have not been consistent with each other. In two studies on MBE grown Cd_3As_2 thin film [35, 37], α is considerably smaller than 0.5. Recently, $\alpha = 1$ was obtained in a slightly Sb doped Cd_3As_2 sample [42], again grown by the MBE technique. On the other hand, in chemical vapor deposition (CVD) grown Cd_3As_2 materials, though weak-antilocalization behaviors have been reported [44, 45], a systematic study of l_ϕ and α has not been carried out.

In this article, we present results from our recent studies of the WAL behaviors at low magnetic fields in a Cd_3As_2 thin flake device. The Hikami–Larkin–Nagaoka (HLN) formula [43] is used to fit the WAL behavior to obtain the phase coherence length l_ϕ and the constant α. It is observed that l_ϕ follows a power law dependence with T, $l_\phi \sim T^{-0.4}$, but tends to saturate to ~180 nm below $T \sim 3$ K. α displays a logarithmic dependence for $T > 3$ K. It, too, tends to saturate below ~3 K. Surprisingly, the saturation value, $\alpha \sim 1.45$, is very close to 1.5, indicating three independent transport channels. We argue that these three independent transport channels are due to the decoupling of three, the top and bottom surfaces as well as the bulk, independent channels. This result, to our knowledge, provides first evidence that the surfaces and bulk states can become decoupled in electronic transport in Dirac semimetal Cd_3As_2.

Cd_3As_2 single crystals are grown in accordance to published methods [46]. Herein, 0.2580 g As powder (3.4×10^{-3} mol, Alfa Aesar, 99.9999% pure) and 1.5501 g Cd powder (1.38×10^{-2} mol, Alfa Aesar, 99.99% pure) were added to a cleaned glass ampoule. The ampoule was cooled and placed under vacuum to 2.0×10^{-5} atm, and torch sealed. The ampoule was then placed in a tube furnace and heated at a ramp rate of 20 °C h^{-1} to 825 °C. It was held at that temperature for 48 h. It was then cooled at a ramp rate of 3 °C h^{-1} to 425 °C, and held for 336 h. At the end of that heating cycle, the ampoule was removed and immediately centrifuged for 3 min at 2000 rpm, then quenched in LN2. Black glassy crystals (0.1–1 mm) were removed from the ampoule, and confirmed for phase purity by single crystal x-ray diffraction: Cd_3As_2, space group = $I4_1/acd$; $a = b = 12.6386(4)$ Å, $c = 25.4077(12)$ Å, $V = 4058.5(3)$ $Å^3$. These lattice parameters are in close agreement with those found in the literature; any discrepancies are minor and may be accounted for within standard errors [46–50]. Figure 1(a) shows an optical image of an as-grown Cd_3As_2 ingot. Figure 1(b) shows an XRD powder pattern simulated from the structural parameters refined from single crystal data.

We follow the procedure in [11] to fabricate our Cd_3As_2 thin flake devices for electronic transport measurements. The size of the flake used is approximately 5 μm × 10 μm. E-beam lithography technique is used to define the ohmic contact pads. A metal stack Ti/Au of 10 nm/200 nm is used to form ohmic contacts to the Cd_3As_2 thin flakes. Low temperature electrical measurements are carried out in an oxford pumped ^{3}He system, with a base temperature of ~0.3 K. By varying the temperatures of its charcoal sorption pump, 1 K pot, and a heater close to the sample, the sample temperature can be varied from 0.3 to ~50 K [51]. A calibrated RuO thermometer, purchased from Scientific Instruments Inc., is used for temperature reading. Four-

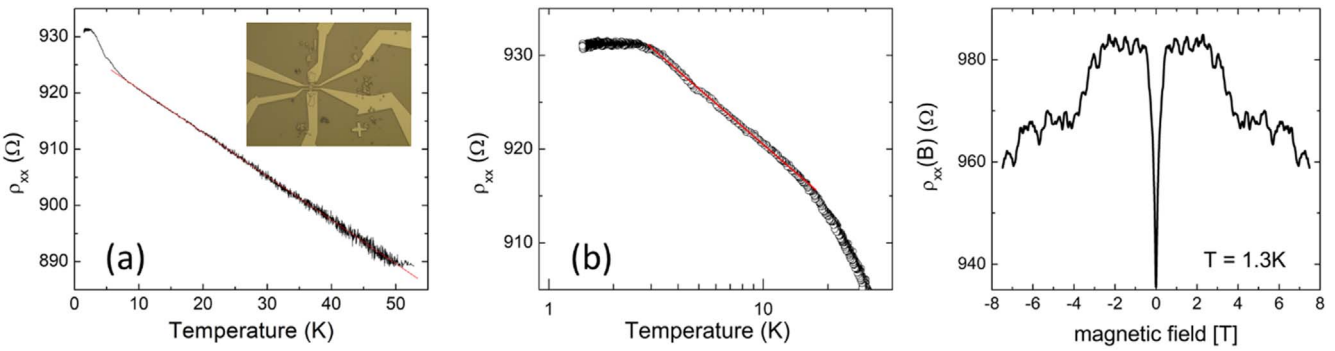

Figure 2. (a) Resistivity as a function of temperature T. The line is a linear fit. The inset shows a photo of the device studied. (b) Resistivity as a function of T in the logarithmic scale. The line is a linear fit, demonstrating the weak localization behavior. (c) Magneto-resistivity at $T = 1.3$ K. The weak-antilocalization cusp behavior is seen around $B = 0$ T.

terminal longitudinal resistance ρ_{xx} and Hall resistance ρ_{xy} are measured using the low-frequency (∼11 Hz) phase lock-in technique. Two Stanford Research Systems Inc. SR830 lock-in amplifiers are used. Lock-in amplifier 1 provides a constant AC voltage (1 V) to induce a current of 10 nA into the sample, through a current-limiting resistor of 100 MΩ (much larger than the sample resistance) [52]. This lock-in amplifier measures ρ_{xx}. The second lock-in amplifier, synchronized with lock-in amplifier 1, measures the Hall resistance ρ_{xy}. At the excitation current of 10 nA, we estimate that electron self-heating is negligible.

Figure 2(a) shows ρ_{xx} as a function of temperature at zero magnetic field. Three regimes with different temperature dependencies are observed. In the temperature range of $10 < T < 50$ K, it is clearly seen that ρ_{xx} follows a linear T dependence and $\rho_{xx} = 928–0.77 \times T$, in units of Ω. Between ∼3 and 10 K, ρ_{xx} displays a logarithmic T dependence, as shown in figure 2(b). This logarithmic temperature dependence is caused by the weak localization effect. Indeed, in a diffusive electron system the destructive quantum interference between two identical self-crossing paths (in which an electron propagates in the opposite directions) leads to an increase in resistivity, which follows a logarithmic temperature dependence [53]. Below 3 K, ρ_{xx} increases at a much slower rate and tends to saturate to a value ∼931 Ω. Figure 2(c) shows the magneto-resistivity $\rho_{xx}(B)$, taken at $T = 1.3$ K, in a large magnetic (B) field range. The pronounced weak-antilocalization cusp near the zero magnetic field is clearly seen, consistent with previous work in topological insulators and semimetals [22–42, 44, 45]. Fluctuations are also observed in magneto-resistivity.

Figures 3(a) and (b) show $\rho_{xx}(B)$ and Hall resistivity $\rho_{xy}(B)$, respectively, around $B = 0$ T at a few selected temperatures. As shown in figure 3(a), the amplitude of fluctuations becomes weaker and eventually disappears at higher temperatures. The Hall resistivity (figure 3(b)) displays a linear B field dependence in the low magnetic fields range around $B = 0$. All the traces overlap with each other, indicating a constant electron density in the temperature range studied. In figure 3(c), we plot the area density n_{2D}, obtained from the slope of $\rho_{xy}(B)$ as a function of temperature. In the temperature range of $0.5 < T < 38$ K, $n_{2D} \sim 1.5 \times 10^{13}$ cm^{-2}. We note that a constant electron density at low temperatures has also been observed before [54]. Moreover, it is believed that a finite electron density in unintentionally doped Cd_3As_2 is due to arsenic vacancies [55]. The 3D density is estimated to be $n_{3D} \sim 7.5 \times 10^{17}$ cm^{-3}, considering the thickness of the thin flake is ∼200 nm. Consequently, the Fermi energy E_F of the system, estimated by using the following formula (equation (2)), is ∼100 meV, which is close to the theoretically calculated Lifshitz transition point [48]

$$E_F = \hbar^2(3\pi^2 n_{3D})^{2/3}/2m^*. \quad (2)$$

Here, the effective electron mass in Cd_3As_2 is taken as $m^* = 0.03$ (in the units of free electron mass).

We caution here that the Fermi energy is calculated based on a simplified model and does not consider the ellipsoid correction [48]. Moreover, there exists a large discrepancy in the literature on the position of the Lifshitz transition point in Cd_3As_2 [6, 10, 48, 56–58]. Theoretically, it was estimated to be ∼130 meV in reference [48]. Experimentally, the measured value differs significantly from one work to another. In [58], it was estimated ∼200 meV using the electronic transport technique. On the other hand, a value of as small as ∼10 meV was estimated in [10] using the STM technique. Understanding the origin of this discrepancy, though extremely important, is beyond the scope of this work. More future studies are needed.

In the following, we will focus on the weak-antilocalization behavior. As shown in figure 3(a), the WAL behavior is weakened as T increases. To analyze the weak-antilocalization effect, we follow the previous practices in topological insulators and topological semimetals and use the HLN formula [43] to analyze the weak-antilocalization effect. In fitting the experimentally measured data, we first convert the resistivity to conductivity, $\sigma_{xx}(B) = \rho_{xx}(B)/(\rho_{xx}(B)^2 + \rho_{xy}(B)^2)$. The magneto-conductivity $\Delta\sigma(B) = \sigma_{xx}(B)–\sigma_{xx}(0)$ is then fitted by the formula (equation (3)):

$$\Delta\sigma(B) = \alpha(e^2/\pi h) \times [\ln(\hbar/4el_\phi{}^2B) - \Psi(1/2 + \hbar/4el_\phi{}^2B)]. \quad (3)$$

In figure 3(d), we show a representative fitting at one temperature of 6.8 K. A good fitting is seen in the low magnetic field range.

We note here that the HLN formula, developed for two-dimensional electron systems (2DES), fits our data well, considering that our device is 200 nm thick. On the other

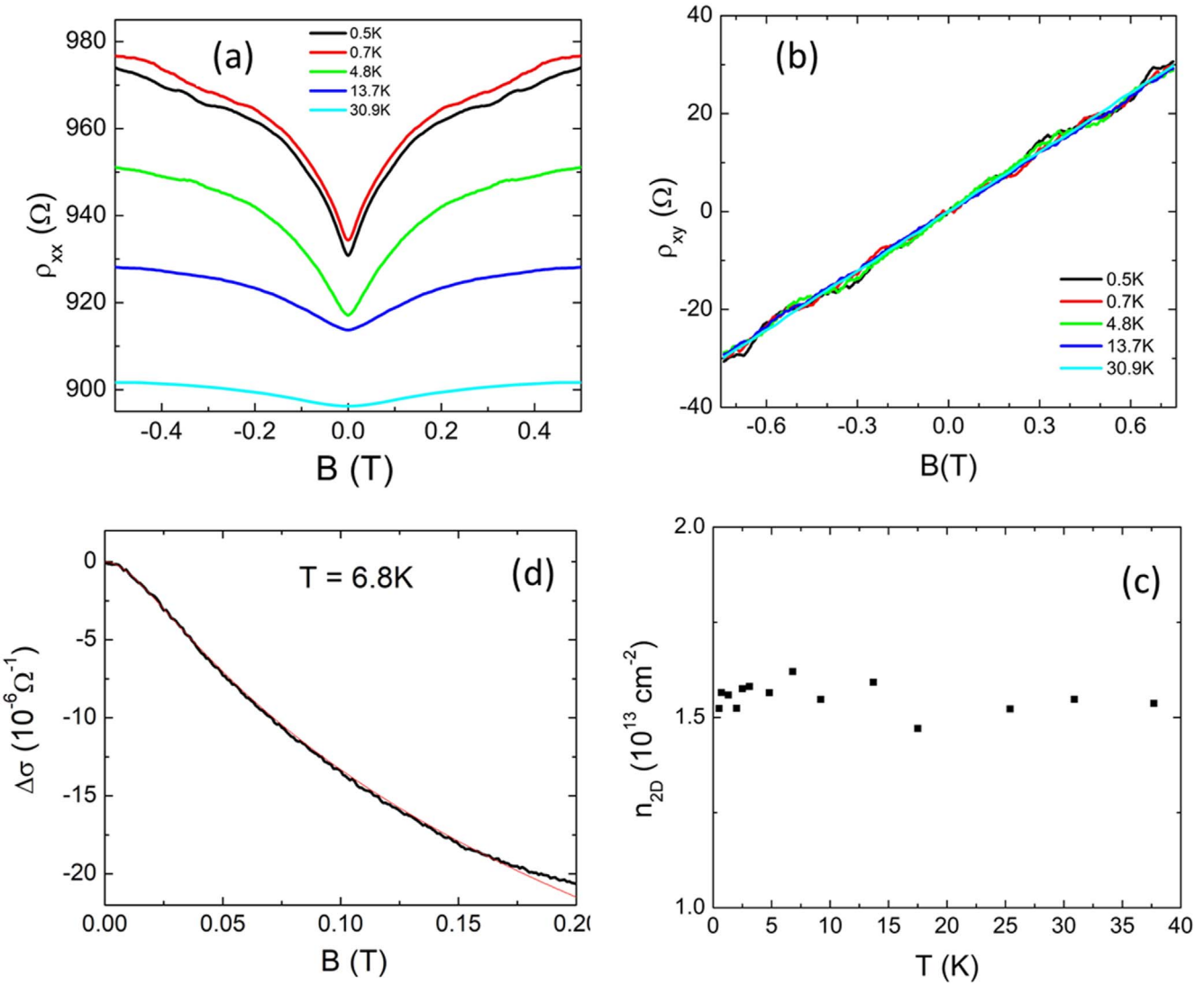

Figure 3. (a) Magneto-resistivity ρ_{xx} around $B = 0$ T at five selected temperatures of 0.5, 0.7, 4.8, 13.7, and 30.9 K. (b) Hall resistivity ρ_{xy} as a function of B at the same selected temperature. Linear B dependence is seen. (c) 2D electron density, obtained from the slope of the linear B dependence of ρ_{xy}, as a function of temperatures. (d) HLN fitting of the weak antilocalization effect at the temperature of 6.8 K.

hand, this is not surprising by comparing the $\rho_{xx}(B)$ data in our specimen (figure 2(c)) with the magneto-resistivity data that are well fitted by a 3D WAL model in [42]. $\rho_{xx}(B)$ in our specimen shows the strong cusp feature typically observed in 2DES. In contrast, the $\rho_{xx}(B)$ data that are well fitted by the 3D WAL model generally shows a quadratic-like B field dependence (see figure 3 in [42]). In fact, the $\rho_{xx}(B)$ curve that shows the cusp feature in their least-doped sample needs to be fitted by the HLN formula, even though the thickness is also about 200 nm (see supplementary materials in [42]). In the following, we discuss a couple of possible mechanisms. First, it is known that the spin–orbit coupling in Cd_3As_2 is strong. As a result, the spin–orbit scattering time can be significantly shorter than the phase coherence time [42] in our specimen. Consequently, the single coherence channel HLN formula can be valid in the bulk [25]. Second, in our specimen, the phase coherence length is on the order of the device thickness (∼200 nm). This can also make the HLN formula a good approximation in fitting the weak-antilocalization effect for the bulk.

In figures 4(a) and (b), we plot the obtained l_ϕ and α as a function of T. l_ϕ follows a power-law temperature dependence in the range of ∼4–40 K, $l_\phi \sim T^{-0.4}$, with a power law coefficient of 0.4, suggesting that electron–electron scattering is the main mechanism for the dephasing process [53] in our device. When T is lower than 3 K, l_ϕ increases at a much slower rate and tends to saturate to a value of ∼180 nm. The value of α also increases with decreasing T and follows a logarithmic dependence between T ∼10 and 40 K (see figure 4(b)). At present, the exact origin of this logarithmic T-depedence is not known. Nevertheless, it indicates that the decoupling of the surfaces and bulk states is a not sudden transition. Rather, it is a gradual process. As T is further reduced below ∼3 K, α also increases at a much slower rate and tends to saturate to a value of ∼1.45. This low-temperature value of 1.45 is larger than 1, suggesting contributions

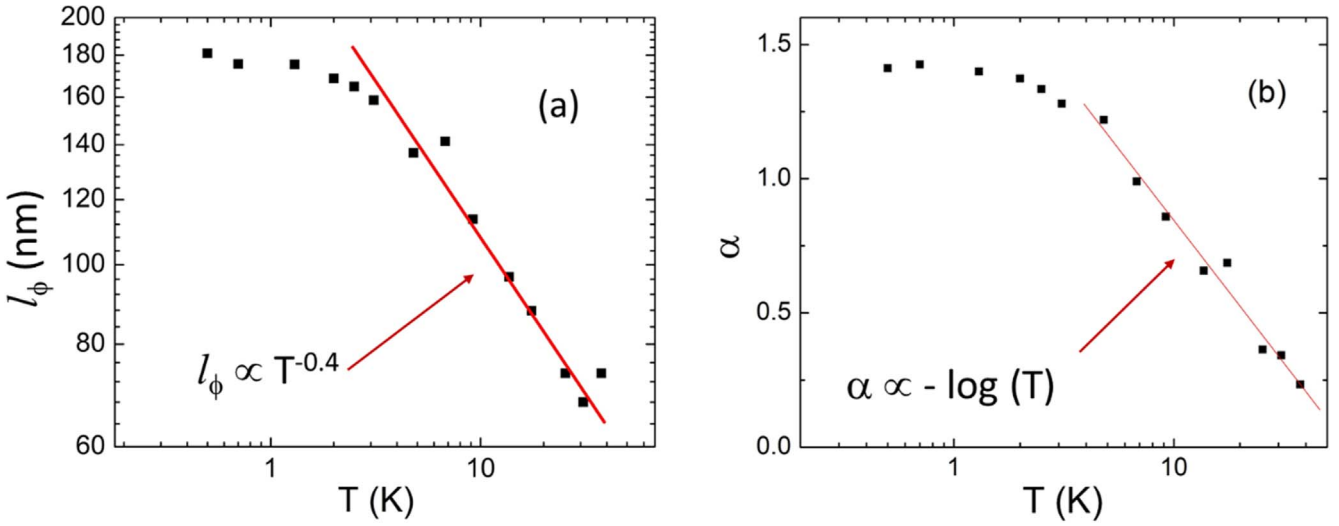

Figure 4. (a) Phase coherence length l_ϕ from the HLN fitting as a function of T. A power-law dependence is observed between 5 and 40 K. l_ϕ saturates to a value of ∼180 nm below 3 K. (b) α as a function of T. It follows a logarithmic T dependence between 5 and 40 K but saturates to a value of 1.45 below 3 K.

from more than two independent channels. Considering it is very close to 1.5, we suggest that at low temperatures there exist three independent parallel channels. In a 3D Dirac semimetal like Cd_3As_2, these three parallel channels can become possible if both the top and bottom surfaces as well as the bulk all become decoupled. Indeed, both the 2D WAL effect from the top and bottom surfaces and the 3D WAL effect have been observed before [23]. Also, independent surface and bulk channels are observed in the studies of Josephson junctions in Cd_3As_2 [11, 12]. Mechanisms other than decoupled surfaces and bulk states might also be possible. For example, the Weyl orbits [59] may contribute to the weak anti-localization effect and cause α to be close to 1.5 in Dirac semimetals. More studies are needed.

Our obtained value of l_ϕ at low temperatures is consistent with that previously reported in Cd_3As_2 samples grown by MBE technique [35, 37]. This seems to suggest that l_ϕ is independent of how the materials is prepared. On the other hand, the value of α is significantly different. In the MBE grown Cd_3As_2 thin films [35, 37], α is considerably less than 0.5. It only approaches to 0.5 at low temperatures [37]. This low value of α is probably due to a small film thickness in their samples, which can result in strong coupling of the two surfaces and bulk. Consequently, only one independent transport channel exists. The asymmetric contribution from the surface and the bulk [26] can further reduce α to a value of less than 0.5. Our Cd_3As_2 thin flake device is significantly thicker. As a result, at low temperatures, the two (top and bottom) surfaces and the bulk can become decoupled and give rise to three independent channels and, thus, a large α value.

It is surprising that all three parameters, the resistivity, l_ϕ and α, tend to saturate below ∼3 K. We speculate that the decoupling of top/bottom surfaces and the bulk may be responsible for the tendency. Indeed, if the bulk-surface scattering is the main mechanism for the sample resistivity in Cd_3As_2 and dephasing of quantum interference, when all three are decoupled, this scattering mechanism is strongly suppressed. Consequently, ρ_{xx}, l_ϕ, and α can saturate to a constant value, respectively. Additional measurements are ongoing to further explore whether and how the decoupling is related to the π phase difference between the surface and bulk states [11].

In conclusion, we have synthesized single crystals of pure Cd_3As_2 and fabricated thin flake devices to measure their electronic transport properties. We present results from our systematic studies of the weak-antilocalization effect. The HLN formula is used to analyze WAL, from which the phase coherence length l_ϕ and the constant α (which is related to independence transport channels) are obtained. It is observed that l_ϕ follows a power law dependence with T at high temperatures, but saturates to ∼180 nm below $T \sim 3$ K. α displays a logarithmic dependence for $T > 3$ K, and saturates below ∼3 K. Surprisingly, the saturation value α is very close to 1.5, indicating three independent transport channels probably due to the decoupling of both the top and bottoms surfaces as well as the bulk states in our Cd_3As_2 thin flake sample. This observation of decoupled surface channels is expected to have important implications for topologically-protected device applications.

We would like to thank Anna Lima-Sharma and James Park for their help and guidance in the Cd_3As_2 crystal growth. The work was supported by a Laboratory Directed Research and Development project at Sandia National Laboratories. Device fabrication was carried out at the Center for Integrated Nanotechnologies, an Office of Science User Facility operated for the U.S. Department of Energy (DOE) Office of Science. Sandia National Laboratories is a multimission laboratory managed and operated by National Technology & Engineering Solutions of Sandia, LLC, a wholly owned subsidiary of Honeywell International Inc., for the U.S. Department of Energy's National Nuclear Security Administration under contract DE-NA0003525. This paper describes objective technical results and analysis. Any subjective views or opinions that might be expressed in the paper do not

necessarily represent the views of the U.S. Department of Energy or the United States Government.

Data availability statement

The data that support the findings of this study are available upon reasonable request from the authors.

ORCID iDs

W Pan https://orcid.org/0000-0002-5629-5296

References

[1] Hasan M Z and Kane C L 2010 Topological insulators *Rev. Mod. Phys.* **82** 3054

[2] Qi X-L and Zhang S-C 2011 Topological insulators and superconductors *Rev. Mod. Phys.* **83** 1057

[3] Armitage N P, Mele E J and Vishwanath A 2018 Weyl and Dirac semimetals in three-dimensional solids *Rev. Mod. Phys.* **90** 015001

[4] Wang A-Q, Ye X-G, Yu D-P and Liao Z-M 2020 Topological Semimetal Nanostructures: From Properties to Topotronics *ACS Nano* **14** 3755

[5] Young S M, Zaheer S, Teo J C Y, Kane C L, Mele E J and Rappe A M 2012 Dirac semimetal in three dimensions *Phys. Rev. Lett.* **108** 140405

[6] Wang Z, Weng H, Wu Q, Dai X and Fang Z 2013 Three-dimensional Dirac semimetal and quantum transport in Cd_3As_2 *Phys. Rev. B* **88** 125427

[7] Borisenko S, Gibson Q, Evtushinsky D, Zabolotnyy V, Büchner B and Cava R J 2014 Experimental realization of a three-dimensional Dirac semimetal *Phys. Rev. Lett.* **113** 027603

[8] Neupane M *et al* 2014 Observation of a three-dimensional topological Dirac semimetal phase in high-mobility Cd_3As_2 *Nat. Commun.* **5** 3786

[9] Liu Z K *et al* 2014 A stable three-dimensional topological Dirac semimetal Cd_3As_2 *Nat. Mater.* **13** 677

[10] Jeon S, Zhou B B, Gyenis A, Feldman B E, Kimchi I, Potter A C, Gibson Q D, Cava R J, Vishwanath A and Yazdani A 2014 Landau quantization and quasiparticle interference in the three-dimensional Dirac semimetal Cd_3As_2 *Nat. Mater.* **13** 851

[11] Yu W, Pan W, Medlin D L, Rodriguez M A, Lee S R, Bao Z-q and Zhang F 2018 π and 4π josephson effects mediated by a Dirac semimetal *Phys. Rev. Lett.* **120** 177704

[12] Wang A-Q, Li C-Z, Li C, Liao Z-M, Brinkman A and Yu D-P 2018 4π-periodic supercurrent from surface states in Cd3As2 nanowire-based josephson junctions *Phys. Rev. Lett.* **121** 237701

[13] Yu W, Haenel R, Rodriguez M A, Lee S R, Zhang F, Franz M, Pikulin D I and Pan W 2020 Zero-bias conductance peak in Dirac semimetal-superconductor devices *Phys. Rev. Res.* **2** 032002

[14] Li C-Z, Wang A-Q, Li C, Zheng W-Z, Brinkman A, Yu D-P and Liao Z-M 2020 Fermi-arc supercurrent oscillations in Dirac semimetal josephson junctions *Nat. Commun.* **11** 1150

[15] Oveshnikov L N, Davydov A B, Suslov A V, Ril' A I, Marenkin S F, Vasiliev A L and Aronzon B A 2020 Superconductivity and shubnikov - de haas effect in polycrystalline Cd_3As_2 thin films *Sci. Rep.* **10** 4601

[16] Zhang S-B, Erdmenger J and Trauzettel B 2018 Chirality josephson current due to a novel quantum anomaly in inversion-asymmetric weyl semimetals *Phys. Rev. Lett.* **121** 226604

[17] Yan Z, Wu Z and Huang W 2020 Vortex end majorana zero modes in superconducting Dirac and weyl semimetals *Phys. Rev. Lett.* **124** 257001

[18] Elliott S R and Franz M 2015 Majorana fermions in nuclear, particle, and solid-state physics *Rev. Mod. Phys.* **87** 137

[19] Lee S R, Sharma P A, Lima-Sharma A L, Pan W and Nenoff T M 2019 Topological quantum materials for realizing majorana quasiparticles *Chem. Mater.* **31** 26

[20] Nayak C, Simon S H, Stern A, Freedman M and Das Sarma S 2008 Non-abelian anyons and topological quantum computation *Rev. Mod. Phys.* **80** 1083

[21] Chatterjee E, Pan W and Soh D 2021 Microwave photon number resolving detector using the topological surface state of superconducting cadmium arsenide *Phys. Rev. Res.* **3** 023046

[22] Chen J *et al* 2010 Gate-voltage control of chemical potential and weak antilocalization in Bi_2Se_3 *Phys. Rev. Lett.* **105** 176602

[23] He H-T, Wang G, Zhang T, Sou I-K, Wong G K L, Wang J-N, Lu H-Z, Shen S-Q and Zhang F-C 2011 Impurity effect on weak antilocalization in the topological insulator Bi_2Te_3 *Phys. Rev. Lett.* **106** 166805

[24] Checkelsky J G, Hor Y S, Cava R J and Ong N P 2011 Bulk band gap and surface state conduction observed in voltage-tuned crystals of the topological insulator Bi_2Se_3 *Phys. Rev. Lett.* **106** 196801

[25] Steinberg H, Laloë J-B, Fatemi V, Moodera J S and Jarillo-Herrero P 2011 Electrically tunable surface-to-bulk coherent coupling in topological insulator thin films *Phys. Rev.* B **84** 233101

[26] Garate I and Glazman L 2012 Weak localization and antilocalization in topological insulator thin films with coherent bulk-surface coupling *Phys. Rev.* B **86** 035422

[27] Liu M *et al* 2012 Crossover between weak antilocalization and weak localization in a magnetically doped topological insulator *Phys. Rev. Lett.* **108** 036805

[28] Taskin A A, Sasaki S, Segawa K and Ando Y 2012 Manifestation of topological protection in transport properties of epitaxial Bi_2Se_3 thin films *Phys. Rev. Lett.* **109** 066803

[29] Bansal N, Kim Y S, Brahlek M, Edrey E and Oh S 2012 Thickness-independent transport channels in topological insulator Bi_2Se_3 thin films *Phys. Rev. Lett.* **109** 116804

[30] Kim D, Syers P, Butch N P, Paglione J and Fuhrer M S 2013 Coherent topological transport on the surface of Bi_2Se_3 *Nat. Commun.* **4** 2040

[31] Lin C J *et al* 2013 Parallel field magnetoresistance in topological insulator thin films *Phys. Rev.* B **88** 041307(R)

[32] Brahlek M, Koirala N, Salehi M, Bansal N and Oh S 2014 Emergence of decoupled surface transport channels in bulk insulating Bi_2Se_3 thin films *Phys. Rev. Lett.* **113** 026801

[33] Li Z *et al* 2015 Experimental evidence and control of the bulk-mediated intersurface coupling in topological insulator Bi_2Te_2Se nanoribbons *Phys. Rev.* B **91** 041401(R)

[34] Lu H-Z and Shen S-Q 2015 Weak antilocalization and localization in disordered and interacting Weyl semimetals *Phys. Rev.* B **92** 035203

[35] Zhao B, Cheng P, Pan H, Zhang S, Wang B, Wang G, Xiu F and Song F 2015 Weak antilocalization in Cd_3As_2 thin films *Sci. Rep.* **6** 22377

[36] Liu W E, Hankiewicz E M and Culcer D 2017 Quantum transport in weyl semimetal thin films in the presence of spin–orbit coupled impurities *Phys. Rev.* B **96** 045307

[37] Schumann T, Galletti L, Kealhofer D A, Kim H, Goyal M and Stemmer S 2018 Observation of the quantum hall effect in confined films of the three-dimensional Dirac semimetal Cd_3As_2 *Phys. Rev. Lett.* **120** 016801
[38] Park H, Chae J, Jeong K, Choi H, Jeong J, Kim D and Cho M-H 2018 Disorder-induced decoupled surface transport channels in thin films of doped topological insulators *Phys. Rev.* B **98** 045411
[39] Fu B, Wang H-W and Shen S-Q 2019 Quantum interference theory of magnetoresistance in Dirac materials *Phys. Rev. Lett.* **122** 246601
[40] Yu L Q, Hu L, Barreda J L, Guan T, He X, Wu K, Li Y Q and Xiong P 2020 Robust gapless surface state against surface magnetic impurities on $(Bi_{0.5}Sb_{0.5})_2Te_3$ evidenced by *In Situ* magnetotransport *Phys. Rev. Lett.* **124** 126601
[41] Niu C, Qiu G, Wang Y, Zhang Z, Si M, Wu W and Ye P D 2020 Gate-tunable strong spin–orbit interaction in two-dimensional tellurium probed by weak antilocalization *Phys. Rev.* B **101** 205414
[42] Nakazawa Y, Uchida M, Nishihaya S, Ohno M, Sato S and Kawasaki M 2021 Enhancement of spin–orbit coupling in Dirac semimetal Cd_3As_2 films by Sb doping *Phys. Rev.* B **103** 045109
[43] Hikami S, Larkin A I and Nagaoka Y 1980 Spin–orbit interaction and magnetoresistance in the two dimensional random system *Prog. Theor. Phys.* **63** 707
[44] Li H, He H, Lu H-Z, Zhang H, Liu H, Ma R, Fan Z, Shen S-Q and Wang J 2016 Negative magnetoresistance in Dirac semimetal Cd_3As_2 *Nat. Commun.* **7** 10301
[45] Zheng W-Z, Ye X-G, Lin B-C, Li R-R, Yu D-P and Liao Z-M 2019 *Appl. Phys. Lett.* **115** 183103
[46] Ali M N, Gibson Q, Jeon S, Zhou B B, Yazdani A and Cava R J 2014 The crystal and electronic structures of Cd3As2, the three-dimensional electronic analogue of graphene *Inorg. Chem.* **53** 4062
[47] Sankar R *et al* 2015 Large single crystal growth, transport property and spectroscopic characterizations of three-dimensional Dirac semimetal Cd_3As_2 *Sci. Rep.* **5** 12966
[48] Feng J, Pang Y, Wu D, Wang Z, Weng H, Li J, Dai X, Fang Z, Shi Y and Lu L 2015 Large linear magnetoresistance in Dirac semimetal Cd_3As_2 with fermi surfaces close to the Dirac points *Phys. Rev.* B **92** 081306(R)
[49] Steigmann G A and Goodyear J 1968 The crystal structure of Cd_3As_2 *Acta Cryst.* B **24** 1062
[50] The lattice constants a,b,c in our single crystal are slightly smaller than those obtained in some CVD grown single crystals, for example, a = b = 12.6512A and c = 25. 4435A in Ref. [47], and a = b = 12.6527A and c = 25. 4578A in Ref. [48]. On the other hand, they are comparable to those in other CVD grown single crystals, for example, a = b = 12.633(3) A, c = 25.427(7)A in Ref. [46], and those in [49]
[51] (https://nationalmaglab.org/images/users/dc_field/searchable_docs/sample_environments/nmr3he/manual.pdf)
[52] (https://www.zhinst.com/americas/en/applications/nanotechnology-materials-science/hall-effect-measurements)
[53] Lee P A and Ramakrishnan T V T V 1985 Disordered electronic systems *Rev. Mod. Phys.* **57** 287
[54] Schumann T, Goyal M, Kealhofer D A and Stemmer S 2017 Negative magnetoresistance due to conductivity fluctuations in films of the topological semimetal Cd_3As_2 *Phys. Rev.* B **95** 241113(R)
[55] Spitzer D P, Castellion G A and Haacke G 1966 Anomalous thermal conductivity of Cd_3As_2 and the Cd_3As_2-Zn_3As_2 Alloys *J. Appl. Phys.* **37** 3795
[56] Hakl M *et al* 2018 Energy scale of Dirac electrons in Cd_3As_2 *Phys. Rev.* B **97** 115206
[57] Krizman G, Schumann T, Tchoumakov T, Assaf B A, Stemmer S, de Vaulchier L A and Guldner Y 2019 Determination of the crystal field splitting energy in Cd_3As_2 using magnetooptics *Phys. Rev* B **100** 155205
[58] Zhao Y *et al* 2015 Anisotropic fermi surface and quantum limit transport in high mobility three-dimensional Dirac semimetal Cd_3As_2 *Phys. Rev. X* **5** 031037
[59] Potter A C, Kimchi I and Vishwanath A 2014 Quantum oscillations from surface Fermi arcs in Weyl and Dirac semimetals *Nat. Commun.* **5** 5161